

USP-Gaussian: Unifying Spike-based Image Reconstruction, Pose Correction and Gaussian Splatting

Kang Chen^{1,2} Jiyuan Zhang^{1,2} Zecheng Hao^{1,2} Yajing Zheng^{1,2,*} Tiejun Huang^{1,2,3} Zhaofei Yu^{1,2,3,*}

¹School of Computer Science, Peking University

²State Key Laboratory for Multimedia Information Processing, Peking University

³Institute for Artificial Intelligence, Peking University

{mrchenkang, jyzhang}@stu.pku.edu.cn, {haozecheng, yj.zheng, tjhuang, yuzf12}@pku.edu.cn

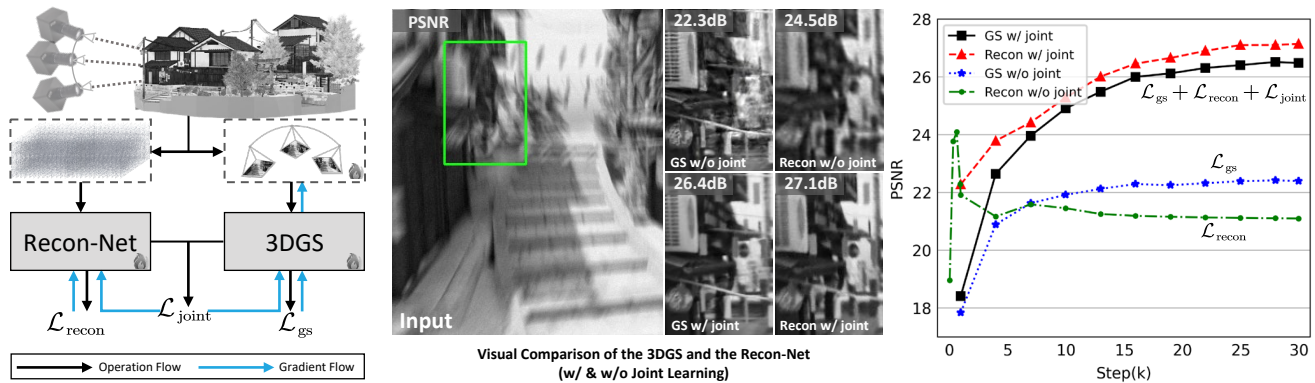


Figure 1. **Left.** Illustration of our USP-Gaussian framework, where the spike-based image reconstruction network (Recon-Net), camera poses, and 3DGS are collaboratively optimized signified by \odot . **Mid.** Visual ablation showcasing the performance of Recon-Net and 3DGS with and without (w/ & w/o) the joint optimization, where the input denotes the long-exposure image formulated by accumulating the spike stream over a period as defined in Eq. (6). **Right.** Training curve comparison for Recon-Net and 3DGS with and without joint optimization.

Abstract

Spike cameras, as an innovative neuromorphic camera that captures scenes with the 0-1 bit stream at 40 kHz, are increasingly employed for the 3D reconstruction task via Neural Radiance Fields (NeRF) or 3D Gaussian Splatting (3DGS). Previous spike-based 3D reconstruction approaches often employ a cascaded pipeline: starting with high-quality image reconstruction from spike streams based on established spike-to-image reconstruction algorithms, then progressing to camera pose estimation and 3D reconstruction. However, this cascaded approach suffers from substantial cumulative errors, where quality limitations of initial image reconstructions negatively impact pose estimation, ultimately degrading the fidelity of the 3D reconstruction. To address these issues, we propose a synergistic optimization framework, *USP-Gaussian*, that unifies spike-based image reconstruction, pose correction, and Gaussian splatting into an end-to-end framework. Lever-

aging the multi-view consistency afforded by 3DGS and the motion capture capability of the spike camera, our framework enables a joint iterative optimization that seamlessly integrates information between the spike-to-image network and 3DGS. Experiments on synthetic datasets with accurate poses demonstrate that our method surpasses previous approaches by effectively eliminating cascading errors. Moreover, we integrate pose optimization to achieve robust 3D reconstruction in real-world scenarios with inaccurate initial poses, outperforming alternative methods by effectively reducing noise and preserving fine texture details. Our code, data and trained models will be available at <https://github.com/chenkang455/USP-Gaussian>.

1. Introduction

Spike cameras [10], inspired by the human retina [44], introduce an innovative paradigm for encoding high-speed dynamic scenes. In contrast to conventional imaging systems [18] that rely on fixed exposure intervals to integrate visual information, spike cameras continuously sense dy-

* Corresponding authors.

namics by recording the spike stream with an impressive firing rate of 40 kHz. Benefiting from the efficient bit representation of spikes, spike cameras can adeptly detect rapid scenes with significantly diminished bandwidth compared to established high-speed cameras such as the Phantom.

Capitalizing on the remarkable capability of the spike camera to capture intricate motion and texture details in high-speed environments, recent research [31, 36, 40, 41, 43, 44] concentrate on its application for high-speed imaging, *i.e.*, establishing the mapping from bit-encoded spike stream to visually perceivable images. Subsequent investigations delve into the estimation of optical flow [38], the enhancement of motion deblur [3, 6, 33] and applications in high-speed object detection [42], semantic segmentation [31], depth estimation [29] and occlusion removal [30].

The Neural Radiance Fields [17] and 3D Gaussian Splatting [11] have emerged as prominent 3D reconstruction technologies in recent years, benefiting from their designed differential training frameworks that map 2D images to 3D representations. 3DGS employs Gaussian primitives for explicit scene representation and the splatting algorithm for projection, thereby achieving faster rendering speed compared to the pixel-by-pixel approach implemented in NeRF. Building on NeRF and 3DGS, the high-speed and continuous capturing potential of the spike camera can be fully unleashed in 3D reconstruction tasks [9, 32, 45].

While the idea of applying the spike camera for 3D reconstruction is trivial and straightforward in a sequential manner, *i.e.*, we can reconstruct images from the spike stream, estimate camera poses and subsequently apply NeRF/3DGS to obtain the 3D representation. Nevertheless, the cascading pipeline introduces significant cumulative errors when the quality of initially recovered images is poor, thereby degrading the accuracy of camera pose estimation and limiting the fidelity of the reconstructed scene.

To this end, SpikeNeRF [45] incorporates a differentiable spike simulator on the outputs of NeRF based on the Spiking Neural Network (SNN), with the loss formulated as the identity between the simulated spike stream and the input spike stream. SpikeGS [32] initiates with a self-supervised Spike-to-Image reconstruction framework built on the Blind Spot Network (BSN) [13], intended to mitigate the performance degradation [4, 5] encountered by supervised learning methods on real-world scenes. With recovered high-quality images, SpikeGS designs a further constraint from the long spike input and integrates it into the 3DGS pipeline. Furthermore, SpikeNVS [7] for rgb-spike multi-modality and Spike-GS [9] for color spike cameras adopt a similar framework, differing only in the input modality. While these works have improved preliminary representation for NeRF/3DGS, they remain constrained within the cascading framework thus inheriting the aforementioned limitation.

To address these challenges, we propose *USP-Gaussian*, Unifying Spike-based image reconstruction, Pose correction, and Gaussian Splatting within a one-stage optimization framework to *mitigate error propagation inherent in three-stage cascading methods*. Specifically, USP-Gaussian comprises two synergistic branches as illustrated in Fig. 1, one dedicated to Spike-to-Image reconstruction via Recon-Net and the other to novel view synthesis implemented with 3DGS. To facilitate the self-supervised training of Recon-Net, we design $\mathcal{L}_{\text{recon}}$ based on the constraint between the input spike stream and recovered outputs. In the 3DGS branch, we develop a spike-based 3DGS framework featuring specially designed loss \mathcal{L}_{gs} , which obviates the requirement for pre-recovered high-quality images and accurate poses. While each branch of USP-Gaussian operates independently, we further introduce the joint loss $\mathcal{L}_{\text{joint}}$ derived from the outputs of both 3DGS and Recon-Net to facilitate unified optimization. Visual ablation comparisons of restored images and the training curve are depicted in Fig. 1, demonstrating that *the joint optimization of the two branches mutually enhances the recovered textures and the overall training process*. We conduct quantitative and qualitative evaluations on the synthetic dataset with accurate pose and the real-world dataset with inaccurate pose estimation. Experiments showcase that our method achieves superior restoration in both datasets, validating the effectiveness of our joint learning framework. In summary, the contributions of our USP-Gaussian are as follows:

- We propose a unified framework for the joint optimization of Recon-Net, Pose, and 3DGS, mitigating error amplification inherent in cascading frameworks.
- We demonstrate that Spike-to-Image and 3D reconstruction tasks can mutually facilitate and enhance the optimization of each other.
- We introduce a novel self-supervised training paradigm for the spike-based image reconstruction network with the multi-view consistency afforded by 3DGS.

2. Related Work

2.1. Spike-based Image Reconstruction

While neuromorphic cameras generate high frame rate bit-stream information, it is imperative to transform them into multi-bit grayscale images that are perceptible to human observers. To achieve this Spike-to-Image target, a plethora of methodologies [4, 5, 31, 36, 40, 41, 44] have been proposed, which can be broadly classified into model-based, supervised, and self-supervised learning paradigms. Model-based methods, rooted in the sampling principle of the spike camera, aim to infer high-fidelity images drawing from the physical spike-image relationship [43], biological retinal models [44], and short-term synaptic plasticity [41]. Confronted with pervasive dark current noise that is challenging

to model, learning-based methods are employed to directly deduce high-frame-rate sharp sequences from spike streams with unknown firing patterns. Specifically, Spk2ImgNet [36] designed a hierarchical architecture engineered to capture the intricate temporal dynamics present within spike streams. Zhao et al. [39] introduced an SNN-based image reconstruction framework SSIR, leveraging the bit-stream sequence processing advantage of the SNN. Concurrently, self-supervised learning methodologies based on the BSN [4, 5] have been developed to counteract the performance deterioration inherent in supervised learning methods stemming from the domain disparity between synthetic and real-world datasets. However, the BSN encounters challenges in effectively removing noise, particularly when the noise levels are pronounced, or images contain abundant textural features.

In this paper, we propose a novel self-supervised spike-based image reconstruction framework that fully exploits the multi-view constraints provided by 3D scenes.

2.2. Novel View Synthesis based on the Neuromorphic Camera

Recent research has extensively employed neuromorphic cameras, including event cameras [8], which encode intensity difference in dynamic scenarios with low-latency and spike cameras [10], for 3D scene reconstruction.

Event Camera. Klenk et al. [12] proposed the E-NeRF based on the event generation mechanism, which can recover sharp 3D scenes under high-speed camera motion. Rudnev et al. [20] further harnessed a color event camera to learn the color representation of scenes. Qi et al. [19] introduced E2NeRF with a multi-modality input, which synthesizes high-quality images of new viewpoints by exploiting the complementary information between the blurry input and the event stream. To fully utilize the motion perception capabilities of event cameras, further research [1, 16] focused on recovering dynamic scenes with rigid deformations from event streams. In addition to NeRF, EvGGs [25] introduces a generalizable Gaussian splatting framework for event cameras designed to reconstruct 3D scenes without retraining. EF-3DGS [14] develops a free-trajectory framework by aligning the RGB input, event streams, and pose. Event3DGS [27] presents an effective solution for rapid ego-motion robotics scenarios.

Spike Camera. Zhu et al. [45] design a differentiable SNN and integrate it into the NeRF training pipeline to simulate the generation of spike streams, where the loss function is formulated based on the rendered spike output and the input spike. Dai et al. [7] further introduce SpikeNVS by extending the spike cameras to RGB-Spike input. Additionally, Guo et al. [9] introduced a color 3D scene reconstruction framework by integrating Bayer-pattern spike streams into the 3DGS training pipeline. SpikeGS [32] initially

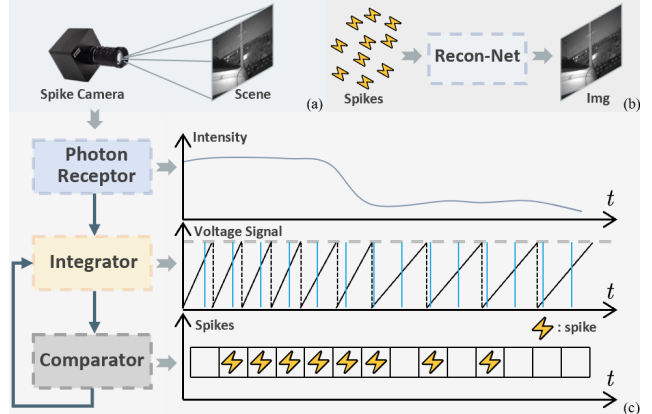


Figure 2. (a) The spike camera captures a railway moving 350 km/h. (b) The Recon-Net is designed to establish the mapping between the input spike stream and the sharp image. (c) The working mechanism of the spike camera.

employs the BSN to recover images from the noisy spike stream and subsequently integrates them into the 3DGS.

While the cascaded framework SpikeGS [32] introduces propagation errors, we propose a joint optimization framework that concurrently handles spike-based image reconstruction, pose estimation, and novel view synthesis.

3. Preliminary

3.1. Spike Camera

The spike camera consists of the photodetector, voltage integrator, comparator, and synchronous readout as shown in Fig. 2. Within the designated time interval $\mathcal{T} = [t_s, t_e]$, the photodetector continuously captures the light intensity $\mathbf{I}(t)$ and converts it into the voltage signal $\mathbf{V}(t) = \mu \mathbf{I}(t)$, where μ is the photoelectric conversion coefficient. Concurrently, the comparator assesses the integrator voltage $\mathbf{A}(t)$ against the predefined threshold Θ . When the threshold is met, the spike is emitted and the integrator voltage is reset, formulated as:

$$\mathbf{A}(t) = \int_{t_s}^t \mathbf{I}(t) dt \bmod C, \quad (1)$$

where $C = \Theta/\mu$ is a constant proportional to the spike firing threshold Θ . While the integrator continuously aggregates voltage, the readout circuit synchronously retrieves spike signals from the registers at up to 40 kHz. Spikes fired during the specified interval \mathcal{T} are represented as a three-dimensional bit stream $\mathcal{S} \in \{0, 1\}^{K \times H \times W}$, where H and W indicate the image height and width, with K denoting the spike sequence length.

3.2. 3D Gaussian Splatting

3D Gaussian Splatting leverages a set of three-dimensional Gaussian primitives, symbolized as $\{\mathcal{G}\}_{n=1}^{N_{gs}}$, to effectively

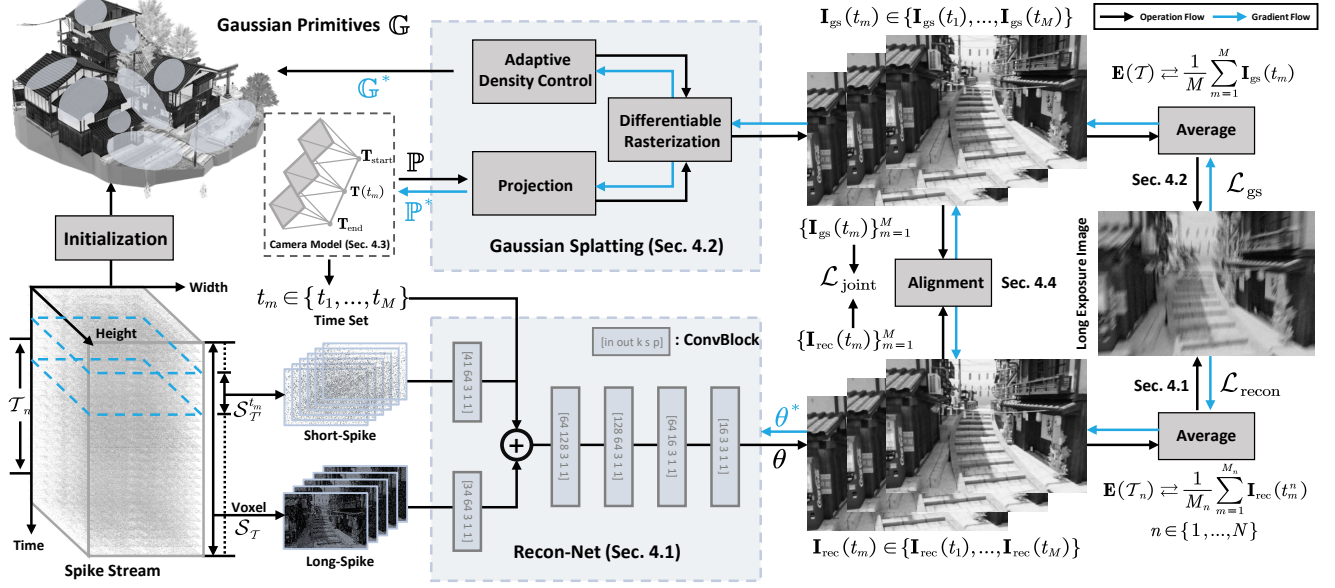


Figure 3. **The working pipeline of our USP-Gaussian.** For each camera viewpoint, we initially derive a pose sequence at equal time intervals based on the camera model described in Sec. 4.3. Leveraging the 3DGS rendering pipeline detailed in Sec. 4.2, we subsequently generate a corresponding sharp image sequence for this viewpoint. Concurrently, Recon-Net is employed to reconstruct a sharp sequence from the captured spike stream as outlined in Sec. 4.1. While Recon-Net and 3DGS are trained based on the discrepancy between the re-synthesized blurry image with the input long-exposure image, alignment of their outputs for the same scene is further enforced through joint optimization loss as described in Sec. 4.4. With formulated loss functions, our USP-Gaussian enables the collaborative optimization of Gaussian primitives, camera poses, and the parameters of Recon-Net as formulated in Eq. (5).

represent the spatial characteristics of the captured scene.

Each Gaussian primitive is centered at a point \mathbf{p}_n , with its spread and orientation influenced by the covariance matrix $\Sigma_n = RSS^T R^T$, where R and T denotes the rotation and the scale matrix, respectively. The impact of the Gaussian on any point \mathbf{v} in the scene is quantified by:

$$\mathcal{G}_n(\mathbf{v}) = \exp\left(-\frac{1}{2}(\mathbf{v} - \mathbf{p}_n)^T \Sigma_n^{-1}(\mathbf{v} - \mathbf{p}_n)\right). \quad (2)$$

When it comes to rendering for viewing transformation W , these 3D Gaussian primitives are mapped onto 2D primitives \mathcal{G}_n^{2D} , with the covariance matrix Σ'_n reformulated as:

$$\Sigma'_n = JW\Sigma_n W^T J^T, \quad (3)$$

where J represents the Jacobian matrix derived from the affine approximation of the projective transformation.

Further, each pixel on the rendered plane is calculated by rasterizing these 2D Gaussians, sorted by depth, according to the following formulation:

$$C(r) = \sum_{k=1}^{N_{\text{gs}}} T_i \alpha_i \mathbf{c}_i, T_i = \prod_{j=1}^{i-1} (1 - \alpha_j), \quad (4)$$

where D represents the indices set reordered by depth, and D_k denotes the index of the Gaussian primitive that is the k -th closest to the rendering point.

4. Methods

Target Clarification. Given spike streams $\{\mathcal{S}_v\}_{v=1}^V$ from V different viewpoints with initial inaccurate poses $\{\mathcal{P}_v\}_{v=1}^V$, the USP-Gaussian is designed to simultaneously optimize the Recon-Net, poses, and Gaussian primitives as shown in Fig. 1, mathematically formulated as:

$$(\mathbb{S}, \mathbb{P}, \mathbb{G}, \theta) \xrightarrow{\text{USP-Gaussian}} (\mathbb{P}^*, \mathbb{G}^*, \theta^*), \quad (5)$$

where \mathbb{S} and \mathbb{P} represent the sets of spike streams and poses from M viewpoints, \mathbb{G} denotes the ensemble of Gaussian primitives, and θ encapsulates the Recon-Net parameters. The notation (*) indicates the optimized parameters.

4.1. Spike-based Image Reconstruction Network

The Recon-Net \mathcal{F} is designed to facilitate the mapping from the spike input to the sharp image as shown in Fig. 2(b), formulated as $\mathbf{I}(f) = \mathcal{F}(\mathcal{S}_{\mathcal{T}}; \theta)$ with f signifying the central moment of the interval \mathcal{T} . Prior research [4, 31, 36] employs a fixed and brief window (41 frames in their configuration) of the spike stream as the network input. However, this representation is insufficient for scenarios with low spike firing rates due to the limited information embedded within.

While extending the window size allows the network to encompass more data from the spike stream, it also compli-

cates feature extraction and demands larger computational models for effective processing. To address it, we configure the input of the Recon-Net with a complementary long-short spike stream as shown in Fig. 3.

Given a long spike stream $\mathcal{S}_{\mathcal{T}}$, we extract a short spike stream $\mathcal{S}_{\mathcal{T}}^t \subset \mathcal{S}_{\mathcal{T}}$ centered around time t , with the network mapping reformulated as $\mathbf{I}(t) = \mathcal{F}(\mathcal{S}_{\mathcal{T}}, \mathcal{S}_{\mathcal{T}}^t, t; \theta)$, where time t is incorporated to guide aligning the short spike within the long spike sequence. Following the event stream pre-processing in [2, 23, 24], we apply voxelization to the long spike stream $\mathcal{S}_{\mathcal{T}}$, reducing its dimensions from $K \times H \times W$ to $\frac{K}{4} \times H \times W$ by accumulating every 4 frame. The network architecture consists of basic convolutional blocks as illustrated in Fig. 3 and detailed in the supplementary materials.

According to the spike camera working mechanism described in Eq. (1), we can reconstruct a long-exposure image $\mathbf{E}(\mathcal{T})$ from the spike input $\mathcal{S}_{\mathcal{T}}$ with the TFP algorithm [43], mathematically formulated as below:

$$\mathbf{E}(\mathcal{T}) = \frac{1}{T} \int_{\mathcal{T}} \mathbf{I}(t) dt = \frac{C \cdot N}{T}, \quad (6)$$

where T denotes the duration of the interval \mathcal{T} , and N is the cumulative number of spikes during this period.

Motivated by the textural similarity between the blurry image and the long-exposure image, we can employ the motion-reblur loss widely employed in self-supervised motion deblurring frameworks [3, 28, 34, 35] to guide the training of the Recon-Net. Building on the Recon-Net, we reconstruct M frames uniformly across the interval to form the image sequence $\{\mathbf{I}_{\text{rec}}(t_m)\}_{m=1}^M$ and average them to synthesize a blurry image with less noise. Further, we can formulate the loss by comparing the synthesized image to the long-exposure spike input, expressed as:

$$\mathbb{L}_{\text{recon}}(M, \mathcal{T}) = \mathcal{L} \left(\frac{1}{M} \sum_{m=1}^M \mathbf{I}_{\text{rec}}(t_m), \mathbf{E}(\mathcal{T}) \right), \quad (7)$$

where the loss function \mathcal{L} combines L_1 loss with a D-SSIM term, defined as $\mathcal{L} = (1 - \lambda)\mathcal{L}_1 + \lambda\mathcal{L}_{\text{D-SSIM}}$, effectively integrating both pixel accuracy and structural similarity.

Nevertheless, the input spike stream $\mathcal{S}_{\mathcal{T}}$ sufficiently captures the information necessary to estimate $\mathbf{E}(\mathcal{T})$ as detailed in Eq. (1), which will lead the Recon-Net to learn a trivial identity mapping. To mitigate it, we fully utilize the continuous representation capability of the spike camera and propose the multiple reblur loss to regularize the reconstructed sequence. Specifically, we extract N sub-intervals from the long exposure $\mathcal{T}_n \subset \mathcal{T}$ with the same central moment as shown in Fig. 3 and apply the reblur loss to each sub-interval, formulating the multi-reblur loss as below:

$$\mathcal{L}_{\text{recon}} = \frac{1}{N} \sum_{n=1}^N \mathbb{L}_{\text{recon}}(M_n, \mathcal{T}_n), \quad (8)$$

where M_n represents the number of reconstructed frames within the n -th sub-interval \mathcal{T}_n .

4.2. Spike-based Gaussian Splatting

Suppose that retrieving the pose for each timestamp within the interval is straightforward. Following Sec. 4.1, we uniformly obtain M poses from the interval \mathcal{T} , yielding a pose sequence $\{\mathbf{T}(t_m)\}_{m=1}^M$ with the corresponding image sequence $\{\mathbf{I}_{\text{gs}}(t_m)\}_{m=1}^M$ rendered via the 3DGS rasterization pipeline as shown in Fig. 3.

While reconstructing a sequence of images from the spike stream by shortening the exposure interval in Eq. (6) for the training of 3DGS sounds feasible, these short-exposure images are noisy and lack texture details [3]. To this end, we utilize the long-exposure image $\mathbf{E}(\mathcal{T})$ as the supervision and design the motion-reblur loss for 3DGS similar to Eq. (7), expressed as:

$$\mathcal{L}_{\text{gs}} = \mathcal{L} \left(\frac{1}{M} \sum_{m=1}^M \mathbf{I}_{\text{gs}}(t_m), \mathbf{E}(\mathcal{T}) \right). \quad (9)$$

4.3. Spike Camera Trajectory Modeling

Building on the learnable pose representation during camera exposure in previous research [26, 37], we employ a similar approach to optimize the camera pose throughout the interval \mathcal{T} as shown in Fig. 3. For each spike stream $\mathcal{S}_{\mathcal{T}}$, we optimize both the start pose $\mathbf{T}_{\text{start}}$ and end pose \mathbf{T}_{end} over the interval, while intermediate poses are represented through interpolation between these two.

For the pose $\mathbf{T}(t_m)$ at time t_m , we utilize linear interpolation in the Lie algebra of $\text{SE}(3)$ to estimate the pose at time t , formulated as:

$$\mathbf{T}(t_m) = \mathbf{T}_{\text{start}} \cdot \exp \left(\frac{t_m}{T} \cdot \log(\mathbf{T}_{\text{start}}^{-1} \cdot \mathbf{T}_{\text{end}}) \right). \quad (10)$$

During the training, the pose set \mathbb{P} consisting of the start and end poses from V viewpoints is jointly optimized with the Recon-Net and Gaussian primitives as in Eq. (5). For further details on the camera trajectory modelling, please refer to BAD-NeRF [26] and BAD-Gaussian [37].

4.4. Joint Optimization

Given the spike stream $\mathcal{S}_{\mathcal{T}}$ along with the start pose $\mathbf{T}_{\text{start}}$ and the end pose \mathbf{T}_{end} to be optimized, we perform evenly spaced sampling interpolation as in Eq. (10) during the interval, obtaining the pose sequence $\{\mathbf{T}(t_m)\}_{m=1}^M$.

For each pose in the sequence, we select a short spike stream centered around the timestamp t_m , obtaining the image sequence $\{\mathbf{I}_{\text{rec}}(t_m)\}_{m=1}^M$ based on the Recon-Net in Sec. 4.1 and the image sequence $\{\mathbf{I}_{\text{gs}}(t_m)\}_{m=1}^M$ rendered from the 3DGS in Sec. 4.2 as shown in Fig. 3. While both

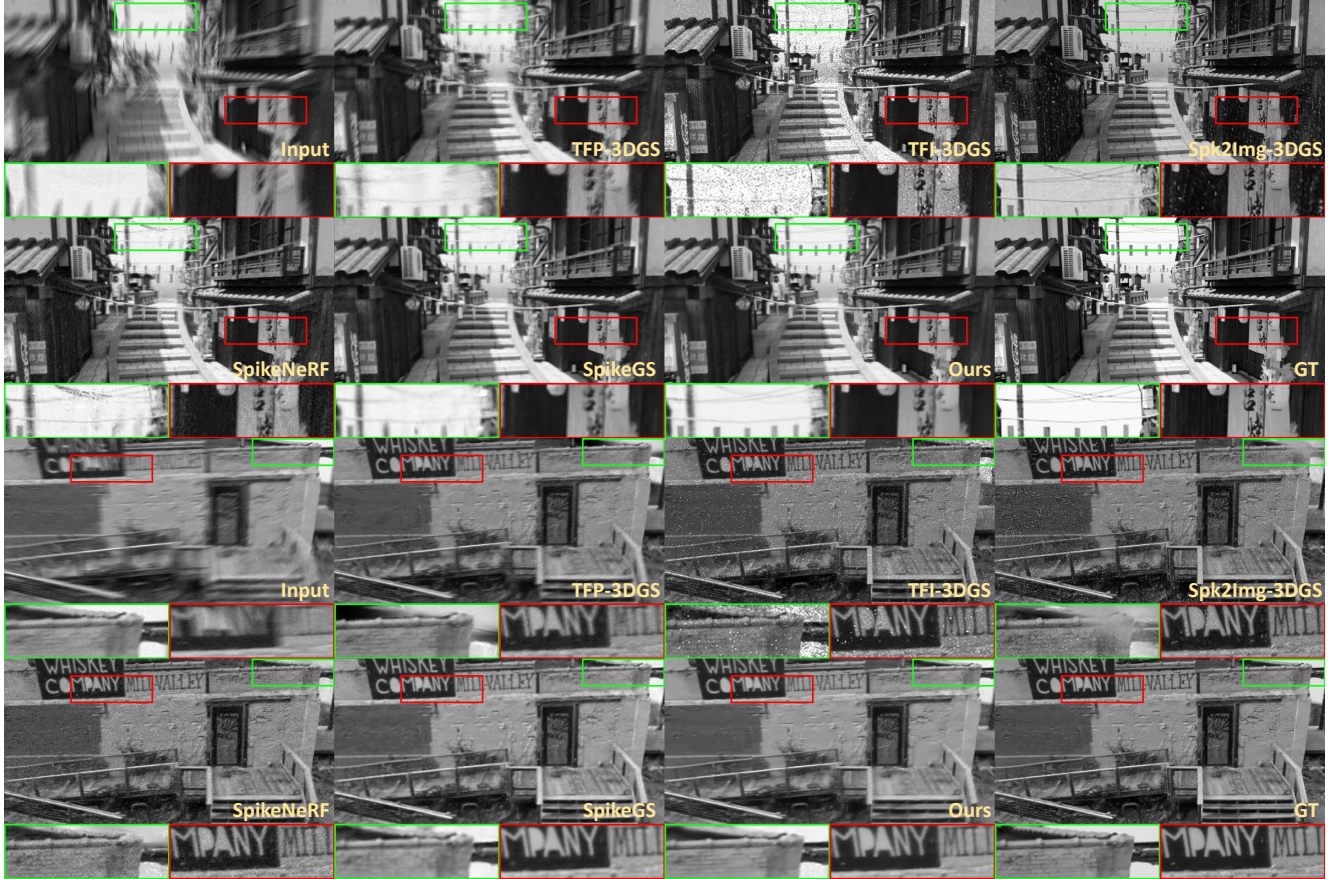


Figure 4. 3D reconstruction visual comparison of our USP-Gaussian compared with previous methods on the synthetic dataset, where the input is the long-exposure image defined in Eq. (6).

sequences represent the same scene, the joint optimization loss $\mathcal{L}_{\text{joint}}$ can be formulated as follows:

$$\mathbb{L}_{\text{joint}} = \frac{1}{M} \sum_{m=1}^M \|\mathbf{I}_{\text{gs}}(t_m) - \mathbf{I}_{\text{rec}}(t_m)\|_2^2. \quad (11)$$

However, we found that the joint optimization framework tends to be unstable due to the order difference between the 3DGS and Recon-Net output sequences. Specifically, since the temporal order does not affect the loss in Eq. (9), the optimized pose sequence may reverse relative to the real camera trajectory. To address this, we apply a simple but effective flip-and-minimum operation to align both sequences, with the loss function reformulated as:

$$\mathcal{L}_{\text{joint}} = \min(\mathbb{L}_{\text{joint}}, \mathbb{L}_{\text{joint}}^{\text{f}}), \quad (12)$$

$$\mathbb{L}_{\text{joint}}^{\text{f}} = \frac{1}{M} \sum_{m=1}^M \|\mathbf{I}_{\text{gs}}(t_{M-m+1}) - \mathbf{I}_{\text{rec}}(t_m)\|_2^2, \quad (13)$$

where the difference between the $\mathbb{L}_{\text{joint}}^{\text{f}}$ and the $\mathbb{L}_{\text{joint}}$ lies in that the rendered sequence via 3DGS is reversed.

To sum up, the loss function for our USP-Gaussian framework is presented as follows:

$$\mathcal{L} = \mathcal{L}_{\text{recon}} + \mathcal{L}_{\text{gs}} + \mathcal{L}_{\text{joint}}. \quad (14)$$

$\mathcal{L}_{\text{recon}}$ optimizes Recon-Net parameters, \mathcal{L}_{gs} refines poses and Gaussian primitives, and $\mathcal{L}_{\text{joint}}$ jointly optimizes all components, with gradient flow shown in Fig. 3.

5. Experiment

5.1. Datasets

Synthetic Dataset. We construct the synthetic dataset based on scenes from Deblur-NeRF [15] for quantitative evaluation. Following the motion trajectory specified in Deblur-NeRF, we start with rendering sharp images at a resolution of 400×600 for each camera viewpoint, with 12 additional intermediate frames inserted between consecutive views. Subsequently, we employ the XVFI [22] to insert 7 images between each frame pair. We employ the spike simulator on the enhanced video sequence to emulate the real-world spike stream as in prior research [3], thus

Table 1. 3D reconstruction quantitative comparison on the synthetic dataset. Color shading indicates the **best** and **second-best** result.

Methods	Wine			Tanabata			Factory			Outdoorpool			Avg		
	PSNR	SSIM	LPIPS	PSNR	SSIM	LPIPS	PSNR	SSIM	LPIPS	PSNR	SSIM	LPIPS	PSNR	SSIM	LPIPS
TFP-3DGS [43]	24.138	0.796	0.239	24.626	0.778	0.274	27.845	0.852	0.179	28.024	0.786	0.294	26.158	0.803	0.239
TFI-3DGS [43]	23.846	0.733	0.251	21.168	0.550	0.529	25.019	0.734	0.278	24.755	0.637	0.446	23.697	0.663	0.376
Spk2Img-3DGS [36]	21.150	0.789	0.178	20.451	0.758	0.214	25.115	0.806	0.143	23.362	0.647	0.417	22.520	0.750	0.238
SpikeNeRF [45]	25.888	0.798	0.200	25.965	0.725	0.295	27.531	0.780	0.191	25.642	0.657	0.396	26.257	0.740	0.270
SpikeGS [32]	25.698	0.835	0.247	26.174	0.826	0.243	28.627	0.864	0.214	28.287	0.797	0.273	27.196	0.832	0.244
Ours	26.476	0.862	0.176	26.300	0.827	0.213	28.694	0.861	0.207	30.142	0.820	0.270	27.903	0.843	0.217

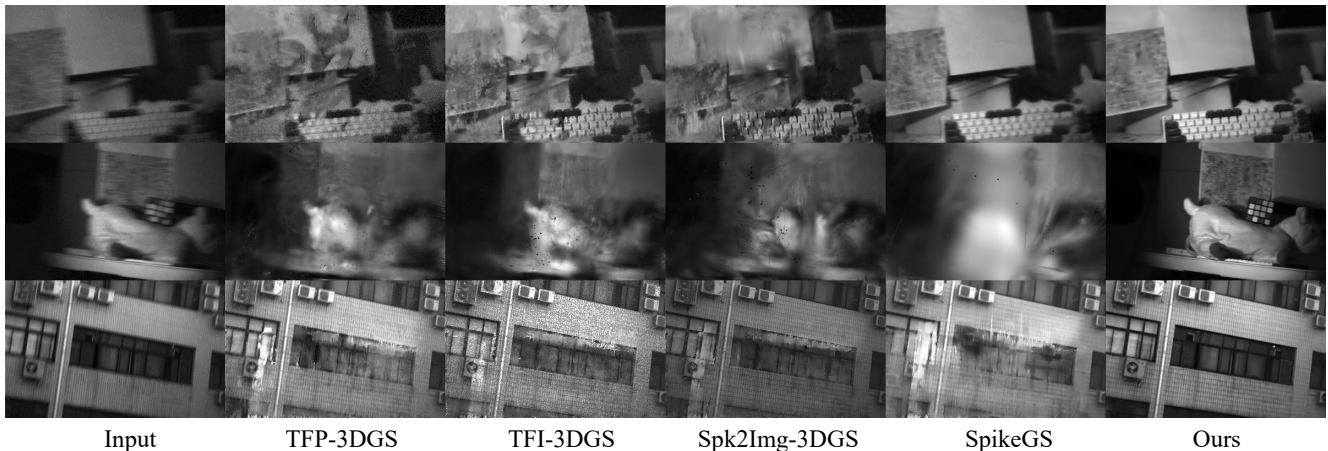


Figure 5. 3D reconstruction visual comparison of our USP-Gaussian compared with previous methods on the real-world dataset, where the input is the long-exposure image defined in Eq. (6).

generating a spike stream of 97 frames for each viewpoint. **Real-world Dataset.** To construct the real-world dataset, we shake the spike camera extremely fast while maintaining a fixed forward-facing orientation and extract 97 spike frames per view, consistent with the configuration in the synthetic dataset. For pose estimation, we convert the raw spike stream in each view to the short-exposure image as defined in Eq. (6) and subsequently employ COLMAP [21] to estimate the pose sequence. Nevertheless, the resulting pose estimates are notably inaccurate due to the substantial noise encoded in the reconstructed sequence.

5.2. Experimental Results

We compare our USP-Gaussian with two-stage cascading pipelines and approaches specially designed for the spike camera, *i.e.*, SpikeNeRF [45] and SpikeGS [32]. For the two-stage approach, we initially apply TFP [43], TFI [43], and Spk2ImgNet [36] to reconstruct sharp images from the input spike, followed by the common 3DGS processing pipeline. All Gaussian-based methods are conducted based on the same 3DGS backbone, and identical camera poses input for a fair comparison. While SpikeGS requires several poses per spike stream for the exposure loss, which presents a notable challenge for COLMAP in real-world data, we omit the exposure loss and retain the rest of the

framework. All comparative metrics are calculated based on the 3D reconstruction task, with further comparison on the Spike-to-Image reconstruction task and implementation details available in the supplementary materials.

Synthetic Dataset. Quantitative and qualitative comparisons on the synthetic dataset are shown in Tab. 1 and Fig. 4 respectively. As illustrated in the Tab. 1, our USP-Gaussian achieves the best performance across most metrics in various scenes. Two-stage cascading methods TFP-3DGS and TFI-3DGS yield poor restoration due to the substantial noise embedded in the initially reconstructed sequence. Similarly, although Spk2ImgNet performs well on its original REDS dataset [36], it experiences substantial degradation due to the dataset domain gap. SpikeGS, as the primary comparison algorithm in this paper, heavily relies on the BSN [13] for self-supervised Spike-to-Image reconstruction. Nevertheless, the denoising performance of the BSN deteriorates in the presence of substantial noise, leading to pronounced grid artifacts and the attenuation of high-frequency details of the SpikeGS. SpikeNeRF faces a comparable challenge, as it requires noisy spike images as input and relies on SNN and NeRF for denoising.

To this end, our proposed collaborative learning framework USP-Gaussian, benefiting from the inherent constraints between the spike stream and the multi-view consis-

Table 2. Quantitative ablation on the synthetic dataset.

ID	\mathcal{L}_{gs}	Recon-Net			3DGS Outputs			Recon-Net Outputs		
		\mathbb{L}_{recon}	\mathcal{L}_{recon}	\mathcal{L}_{joint}	PSNR	SSIM	LPIPS	PSNR	SSIM	LPIPS
I	✓				22.392	0.750	0.208	24.255	0.708	0.358
II		✓						24.567	0.744	0.332
III			✓					25.571	0.807	0.244
IV	✓	✓		✓	25.659	0.850	0.184	27.138	0.855	0.178
V	✓		✓	✓	26.476	0.862	0.176			

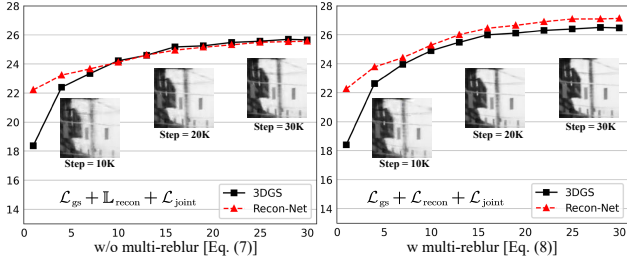


Figure 6. Visual ablation on the effectiveness of multi-reblur loss, with the x-axis and y-axis representing step (k) and PSNR.

tency afforded by the 3DGS, effectively addresses the aforementioned problems without relying on the pre-training of the spike-based image reconstruction network.

Real-world Dataset. While we have demonstrated the advantages of joint learning between 3DGS and Recon-Net on the synthetic dataset, we further conduct the visual comparison on real-world data in Fig. 5, to highlight the necessity of correcting pose during the optimization. Due to the rapid camera ego-motion and the low imaging quality of the spike camera characterized by low spatial resolution, insufficient texture details, and underexposure, the pose sequence estimated by the COLMAP is highly inaccurate, presenting significant challenges for sequential-based methods to recover captured 3D scene. As observed in Fig. 5, baseline methods fail to reconstruct the corresponding scene owing to the improper pose representation, while our USP-Gaussian overcomes this limitation by benefiting from the unifying optimization of the pose.

5.3. Ablation Study

In this subsection, we demonstrate the effectiveness of our proposed joint optimization, complementary spike input, and multi-reblur loss strategies.

Joint Learning. The highlight of USP-Gaussian lies in the design of the joint loss, which aligns outputs from the 3DGS and Recon-Net thus achieving complementary performance improvement. We conduct the ablation experiment on loss functions of \mathcal{L}_{gs} , \mathcal{L}_{recon} and \mathcal{L}_{joint} with quantitative results listed in Tab. 2. As illustrated in the table, the incorporation of the joint loss (ID-V) yields notable improvements in PSNR (18.24%/11.89%), SSIM (14.93%/20.76%), and LPIPS (15.38%/50.28%) for both 3DGS and Recon-Net compared to independent optimiza-

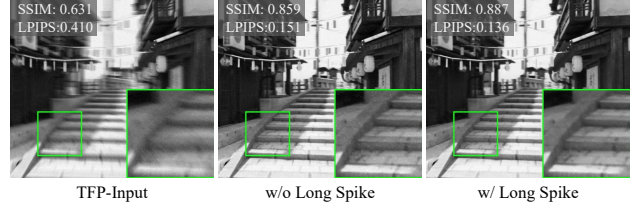


Figure 7. Visual ablation on the effectiveness of long spike input.

tion ((ID-I and ID-III).

Further visual ablation comparisons of the restored image and the training curve are presented in Fig. 1. Visual comparison substantiates that the joint optimization of GS and Recon-Net significantly enhances the texture details for both two. Regarding the training curve, the independent 3DGS training (ID-I) demonstrates slow convergence due to the absence of crucial information in the long-exposure images. Concurrently, the independent training of Recon-Net (ID-III) tends to overfit due to the simplicity of the spike reconstruction task coupled with the limited constraint from self-supervised loss. To this end, our proposed joint optimization framework provides synergistic benefits for both, *i.e.*, Recon-Net effectively compensates for deficient motion features embedded in the long-exposures image while the multi-view consistency afforded by 3DGS culminates in coherent outputs from the Recon-Net. The training curve in Fig. 1 further demonstrates the synergistic optimization process of Recon-Net and 3DGS.

Multi-reblur Loss. The multi-reblur loss \mathcal{L}_{recon} in Eq. (7) is designed to substitute the single-reblur loss \mathbb{L}_{recon} in Eq. (8). Without further constraints, \mathbb{L}_{recon} will lead Recon-Net to learn an identity mapping from the input spike stream to the corresponding long-exposure image as demonstrated in [3]. Comparative analysis in Tab. 2 depicts that \mathcal{L}_{recon} (ID-V) yields beneficial improvement than \mathbb{L}_{recon} (ID-IV). Further comparison on the training curve in Fig. 6 reveals the mechanism of collaborative training, *i.e.*, the multi-reblur loss enhances the performance of Recon-Net, thereby facilitating the 3DGS training.

Complementary Input. We utilize complementary long and short spike stream inputs for Recon-Net to address the fixed short window limitation inherent in previous methods [4, 31, 36]. As illustrated in the visual comparison in Fig. 7, within the same joint optimization framework, the inclusion of long spike stream inputs effectively suppresses salt-and-pepper noise in the output of the reconstruction network, leading to improved SSIM and LPIPS metrics.

6. Conclusion

In this paper, we propose a unifying framework USP-Gaussian for the collaborative optimization of spike-based image reconstruction, pose correction, and Gaussian Splat-

ting. By mitigating error propagation inherent in traditional cascading frameworks, USP-Gaussian attains high reconstruction fidelity across both synthetic and real-world datasets, with further ablation experiments revealing that Spike-to-Image reconstruction and 3D reconstruction tasks furnish mutually complementary information.

References

- [1] Anish Bhattacharya, Ratnesh Madaan, Fernando Cladera, Sai Vemprala, Rogerio Bonatti, Kostas Daniilidis, Ashish Kapoor, Vijay Kumar, Nikolai Matni, and Jayesh K Gupta. Evidnerf: Reconstructing event data with dynamic neural radiance fields. In *WACV*, pages 5846–5855, 2024. 3
- [2] Kang Chen and Lei Yu. Motion deblur by learning residual from events. *IEEE TMM*, 2024. 5
- [3] Kang Chen, Shiyuan Chen, Jiyuan Zhang, Baoyue Zhang, Yajing Zheng, Tiejun Huang, and Zhaofei Yu. Spikereveal: Unlocking temporal sequences from real blurry inputs with spike streams. *arXiv preprint arXiv:2403.09486*, 2024. 2, 5, 6, 8
- [4] Shiyuan Chen, Chaoteng Duan, Zhaofei Yu, Ruiqin Xiong, and Tiejun Huang. Self-supervised mutual learning for dynamic scene reconstruction of spiking camera. In *IJCAI*, pages 2859–2866, 2022. 2, 3, 4, 8
- [5] Shiyuan Chen, Zhaofei Yu, and Tiejun Huang. Self-supervised joint dynamic scene reconstruction and optical flow estimation for spiking camera. In *AAAI*, pages 350–358, 2023. 2, 3
- [6] Shiyuan Chen, Jiyuan Zhang, Yajing Zheng, Tiejun Huang, and Zhaofei Yu. Enhancing motion deblurring in high-speed scenes with spike streams. In *NeurIPS*, 2023. 2
- [7] Gaole Dai, Zhenyu Wang, Qinwen Xu, Wen Cheng, Ming Lu, Boxing Shi, Shanghang Zhang, and Tiejun Huang. Spikenvs: Enhancing novel view synthesis from blurry images via spike camera. *arXiv preprint arXiv:2404.06710*, 2024. 2, 3
- [8] Guillermo Gallego, Tobin Delbrück, Garrick Orchard, Chiara Bartolozzi, Brian Taba, Andrea Censi, Stefan Leutenegger, Andrew J Davison, Jörg Conradt, Kostas Daniilidis, et al. Event-based vision: A survey. *IEEE TPAMI*, 44(1):154–180, 2020. 3
- [9] Yijia Guo, Liwen Hu, Lei Ma, and Tiejun Huang. Spikegs: Reconstruct 3d scene via fast-moving bio-inspired sensors. *arXiv preprint arXiv:2407.03771*, 2024. 2, 3
- [10] Tiejun Huang, Yajing Zheng, Zhaofei Yu, Rui Chen, Yuan Li, Ruiqin Xiong, Lei Ma, Junwei Zhao, Siwei Dong, Lin Zhu, et al. 1000× faster camera and machine vision with ordinary devices. *Engineering*, 25:110–119, 2023. 1, 3
- [11] Bernhard Kerbl, Georgios Kopanas, Thomas Leimkühler, and George Drettakis. 3d gaussian splatting for real-time radiance field rendering. *ACM Trans. Graph.*, 42(4):139–1, 2023. 2
- [12] Simon Klenk, Lukas Koestler, Davide Scaramuzza, and Daniel Cremers. E-nerf: Neural radiance fields from a moving event camera. *IEEE Robotics and Automation Letters*, 8(3):1587–1594, 2023. 3
- [13] Samuli Laine, Tero Karras, Jaakko Lehtinen, and Timo Aila. High-quality self-supervised deep image denoising. *NeurIPS*, 32, 2019. 2, 7
- [14] Bohao Liao, Wei Zhai, Zengyu Wan, Tianzhu Zhang, Yang Cao, and Zheng-Jun Zha. Ef-3dgs: Event-aided free-trajectory 3d gaussian splatting. *arXiv preprint arXiv:2410.15392*, 2024. 3
- [15] Li Ma, Xiaoyu Li, Jing Liao, Qi Zhang, Xuan Wang, Jue Wang, and Pedro V Sander. Deblur-nerf: Neural radiance fields from blurry images. In *CVPR*, pages 12861–12870, 2022. 6
- [16] Qi Ma, Danda Pani Paudel, Ajad Chhatkuli, and Luc Van Gool. Deformable neural radiance fields using rgb and event cameras. In *ICCV*, pages 3590–3600, 2023. 3
- [17] Ben Mildenhall, Pratul P. Srinivasan, Matthew Tancik, Jonathan T. Barron, Ravi Ramamoorthi, and Ren Ng. Nerf: Representing scenes as neural radiance fields for view synthesis. In *ECCV*, 2020. 2
- [18] Bryan Peterson. *Understanding exposure: how to shoot great photographs with any camera*. AmPhoto books, 2016. 1
- [19] Yunshan Qi, Lin Zhu, Yu Zhang, and Jia Li. E2nerf: Event enhanced neural radiance fields from blurry images. In *ICCV*, pages 13254–13264, 2023. 3
- [20] Viktor Rudnev, Mohamed Elgharib, Christian Theobalt, and Vladislav Golyanik. Eventnerf: Neural radiance fields from a single colour event camera. In *CVPR*, pages 4992–5002, 2023. 3
- [21] Johannes L Schonberger and Jan-Michael Frahm. Structure-from-motion revisited. In *CVPR*, pages 4104–4113, 2016. 7
- [22] Hyeonjun Sim, Jihyong Oh, and Munchurl Kim. Xvfi: extreme video frame interpolation. In *ICCV*, pages 14489–14498, 2021. 6
- [23] Chen Song, Qixing Huang, and Chandrajit Bajaj. E-cir: Event-enhanced continuous intensity recovery. In *CVPR*, pages 7803–7812, 2022. 5
- [24] Bishan Wang, Jingwei He, Lei Yu, Gui-Song Xia, and Wen Yang. Event enhanced high-quality image recovery. In *ECCV*, pages 155–171. Springer, 2020. 5
- [25] Jiaxu Wang, Junhao He, Ziyi Zhang, Mingyuan Sun, Jingkai Sun, and Renjing Xu. Evggs: A collaborative learning framework for event-based generalizable gaussian splatting. *arXiv preprint arXiv:2405.14959*, 2024. 3
- [26] Peng Wang, Lingzhe Zhao, Ruijie Ma, and Peidong Liu. Bad-nerf: Bundle adjusted deblur neural radiance fields. In *CVPR*, pages 4170–4179, 2023. 5
- [27] Tianyi Xiong, Jiayi Wu, Botao He, Cornelia Fermüller, Yiannis Aloimonos, Heng Huang, and Christopher Metzler. Event3dgs: Event-based 3d gaussian splatting for high-speed robot egomotion. In *8th Annual Conference on Robot Learning*, 2024. 3
- [28] Fang Xu, Lei Yu, Bishan Wang, Wen Yang, Gui-Song Xia, Xu Jia, Zhendong Qiao, and Jianzhuang Liu. Motion deblurring with real events. In *ICCV*, pages 2583–2592, 2021. 5
- [29] Jiyuan Zhang, Lulu Tang, Zhaofei Yu, Jiwen Lu, and Tiejun Huang. Spike transformer: Monocular depth estimation for spiking camera. In *ECCV*, pages 34–52. Springer, 2022. 2

- [30] Jiyuan Zhang, Shiyuan Chen, Yajing Zheng, Zhaofei Yu, and Tiejun Huang. Unveiling the potential of spike streams for foreground occlusion removal from densely continuous views. *arXiv preprint arXiv:2307.00821*, 2023. 2
- [31] Jiyuan Zhang, Shanshan Jia, Zhaofei Yu, and Tiejun Huang. Learning temporal-ordered representation for spike streams based on discrete wavelet transforms. In *AAAI*, pages 137–147, 2023. 2, 4, 8
- [32] Jiyuan Zhang, Kang Chen, Shiyuan Chen, Yajing Zheng, Tiejun Huang, and Zhaofei Yu. Spikegs: 3d gaussian splatting from spike streams with high-speed camera motion. *arXiv preprint arXiv:2407.10062*, 2024. 2, 3, 7
- [33] Jiyuan Zhang, Shiyuan Chen, Yajing Zheng, Zhaofei Yu, and Tiejun Huang. Spike-guided motion deblurring with unknown modal spatiotemporal alignment. In *CVPR*, pages 25047–25057, 2024. 2
- [34] Xiang Zhang and Lei Yu. Unifying motion deblurring and frame interpolation with events. In *CVPR*, pages 17765–17774, 2022. 5
- [35] Xiang Zhang, Lei Yu, Wen Yang, Jianzhuang Liu, and Gui-Song Xia. Generalizing event-based motion deblurring in real-world scenarios. In *ICCV*, pages 10734–10744, 2023. 5
- [36] Jing Zhao, Ruiqin Xiong, Hangfan Liu, Jian Zhang, and Tiejun Huang. Spk2imgnet: Learning to reconstruct dynamic scene from continuous spike stream. In *CVPR*, pages 11996–12005, 2021. 2, 3, 4, 7, 8
- [37] Lingzhe Zhao, Peng Wang, and Peidong Liu. Bad-gaussians: Bundle adjusted deblur gaussian splatting. *arXiv preprint arXiv:2403.11831*, 2024. 5
- [38] Rui Zhao, Ruiqin Xiong, Jing Zhao, Zhaofei Yu, Xiaopeng Fan, and Tiejun Huang. Learning optical flow from continuous spike streams. *NeurIPS*, 35:7905–7920, 2022. 2
- [39] Rui Zhao, Ruiqin Xiong, Jian Zhang, Zhaofei Yu, Shuyuan Zhu, Lei Ma, and Tiejun Huang. Spike camera image reconstruction using deep spiking neural networks. *IEEE Transactions on Circuits and Systems for Video Technology*, 2023. 3
- [40] Rui Zhao, Ruiqin Xiong, Jing Zhao, Jian Zhang, Xiaopeng Fan, Zhaofei Yu, and Tiejun Huang. Boosting spike camera image reconstruction from a perspective of dealing with spike fluctuations. In *CVPR*, pages 24955–24965, 2024. 2
- [41] Yajing Zheng, Lingxiao Zheng, Zhaofei Yu, Boxin Shi, Yonghong Tian, and Tiejun Huang. High-speed image reconstruction through short-term plasticity for spiking cameras. In *CVPR*, pages 6358–6367, 2021. 2
- [42] Yajing Zheng, Zhaofei Yu, Song Wang, and Tiejun Huang. Spike-based motion estimation for object tracking through bio-inspired unsupervised learning. *IEEE TIP*, 32:335–349, 2022. 2
- [43] Lin Zhu, Siwei Dong, Tiejun Huang, and Yonghong Tian. A retina-inspired sampling method for visual texture reconstruction. In *ICME*, pages 1432–1437. IEEE, 2019. 2, 5, 7
- [44] Lin Zhu, Siwei Dong, Jianing Li, Tiejun Huang, and Yonghong Tian. Retina-like visual image reconstruction via spiking neural model. In *CVPR*, pages 1438–1446, 2020. 1, 2
- [45] Lin Zhu, Kangmin Jia, Yifan Zhao, Yunshan Qi, Lizhi Wang, and Hua Huang. Spikenerf: Learning neural radiance fields from continuous spike stream. In *Proceedings of the IEEE/CVF Conference on Computer Vision and Pattern Recognition*, pages 6285–6295, 2024. 2, 3, 7